Fatigue & Fracture of Engineering Materials & Structures

WILEY

FFEMS Fatigue & Fracture of Engineering Materials & Structures

ORIGINAL ARTICLE OPEN ACCESS

An Experimental Study on the Fatigue Response of Hybrid Additively Manufactured 1.2343 Hot Work Steel - MARAGING Steel MS1

Dario Croccolo[1] | Snežana Ćirić-Kostić[2] | Massimiliano De Agostinis[1] | Stefano Fini[1] | Mattia Mele[1] | Nebojša Bogojević[2] | Vladimir Sinđelić[2] | Giorgio Olmi[1]

[1]Department of Industrial Engineering (DIN), University of Bologna, Bologna, Italy | [2]Faculty of Mechanical and Civil Engineering in Kraljevo, University of Kragujevac, Serbia

Correspondence: Giorgio Olmi (giorgio.olmi@unibo.it)

Received: 31 July 2024 | **Revised:** 12 January 2025 | **Accepted:** 30 January 2025

Funding: This project has received funding from the European Union's Horizon 2020 research and innovation program under the Marie Skłodowska-Curie grant agreement no. 734455: The authors wish to acknowledge the financial support by the European Commission.

Keywords: 1.2343 hot work steel | bi-metal component | fatigue | hybrid additive manufacturing | maraging steel MS1

ABSTRACT

Hybrid additive manufacturing consists of upgrading wrought material by an additive process, adding stacked layers through the melting and sintering of a different material powder. A literature survey indicates that fatigue data for hybrid additively manufactured parts are currently missing. This paper is focused on the fatigue response of 1.2343 hot work steel, upgraded by a maraging steel MS1 powder processed by laser powder bed fusion, and finally heat-treated complying with the specifications from the powder supplier. Results, supported by microscopy SEM analyses, indicate the fatigue response is significantly reduced if compared to that of plain additively manufactured MS1. This is due to the joint between the two materials acting as a weak point, where the porosity of MS1 is incremented with respect to specifications. Moreover, due to the unavailability of a heat treatment that is suitable for both the involved materials, the hot work steel side exhibits poor hardness.

1 | Introduction

To date, it is firmly established that additive manufacturing (AM) technologies offers significant new opportunities in the design of industrial products. Specifically, various AM technologies facilitate the production of a wide array of metal alloys characterized by considerable mechanical performance, thereby enabling the manufacturing of structural parts [1]. Despite the unprecedented design possibilities offered by these processes, several factors continue to constrain their practical application. More specifically, the primary limitations include extended build times, restricted build volumes, and inadequate surface quality of the manufactured parts [2]. In order to address these constraints, numerous studies have investigated the integration of additive manufacturing into conventionally manufactured parts. This approach aims to leverage the advantages of both conventional and innovative technologies and falls under the classification of hybrid additive manufacturing (HAM). Different combinations of AM and conventional technologies, along with diverse materials, can be applied in HAM [3, 4]. A review conducted by Popov et al. [5] outlined that the most applied processes in the HAM of steels are direct energy deposition (DED) and laser powder bed fusion (LPBF). DED can be integrated into a five-axis computer numerical control (CNC) working center, enabling the alternating deposition of material and milling operations. Conversely, LPBF is confined to planar construction, limiting its adaptability to complicated geometries [3]. However, LPBF stands as the predominant AM technology within the metal AM market, as it offers superior surface resolution and reduced internal porosity in the manufactured

https://doi.org/10.1111/ffe.14602

Summary

- Studies on the fatigue response of hybrid additively manufactured parts are lacking.
- The porosity level is high at the bimetal interface, which worsens the fatigue response.
- Issues arise from different heat treatments being needed by the connected materials.
- A transition from ductile to brittle fracture is observed at the joint, where most fractures occurred.

parts [6]. Consequently, research focusing on the combination of LPBF and the conventional manufacturing processes in HAM holds a significant interest in the industry field.

A few studies have been conducted on LPBF of parts on a substrate made of the same material and manufactured by conventional technologies for Co-Cr-Mo [7], AISI 316L [8], and Ti6Al4V [9–11]. These studies yield consistent results supporting the outcome that the LPBF process enables the attainment of a high-quality bond between the two components. This conclusion is always confirmed by microscopy observations. Furthermore, both tensile and torsion tests conducted in these studies resulted in fractures occurring far from the joining region, which was further proof of the strength of this joined structure being well comparable or even greater than that of the base material [8].

The combination of different materials holds significant importance, as it allows for the functionalization of the physical properties of the final part [12]. Specifically, considerable attention has been directed towards the HAM of maraging steels due to the numerous tooling applications associated with these alloys [13].

Tan et al. [14] explored the feasibility of additive manufacturing an MS1 part on a copper substrate. Their scanning electron microscope (SEM) observations revealed a defect-free interface between the two materials. Additionally, both tensile and bending tests conducted on the final parts indicated that failure occurred on the copper side, away from the interface region. Expanding upon this work, Kucerova et al. furthered the investigation to encompass different substrate materials: CMnAlNb steel [15], maraging steel VACO 180 [16], and 42SiCr [17]. Across all these alloys, the researchers conducted SEM observations of the interface and performed tensile tests on the final parts. Their findings consistently demonstrated a high-quality interface bonding in all cases, with specimen fracture occurring within the base material.

Considerable attention has been directed towards researching the HAM of maraging steel and hot work steel (HWS) due to the similarity in their mechanical characteristics [5]. Azizi et al. [18] presented findings on the HAM of MS1 maraging steel on an H13 (corresponding to DIN 1.2344 tool steel) substrate. They demonstrated that by adjusting the heat treatment, similar properties to those of the wrought MS1 material could be achieved. However, unlike the outcomes of the previous studies, their results indicated a high porosity at the interface between the additively manufactured and wrought material. Moreover, microstructural and chemical inhomogeneities in the bonding region led to specimen fracture occurring at the interface between the two materials.

A similar investigation analyzing HAM of MS1 and H13 via LPBF was conducted in the same year by Shakerin et al. [19]. The problem arising from different heat treatment procedures being needed for alloyed steels (such as MS1) versus tool steels with high carbon composition is highlighted. Interestingly, their results contradicted those of Azizi et al. [18], as the fracture of the tensile specimen occurred in the H13 substrate, far from the interface. Shakerin et al. [20] further explored the tensile and bending behavior of MS1 steel HAM on a low-alloy tool steel, specifically P20. Consistently with the previous study, the authors observed crack initiation and propagation in the tool steel substrate, indicating that the interface between the two materials did not seem to be the critical region affecting the final component.

The studies referenced above offer insights into the static mechanical properties of components produced by HAM using LPBF. However, it worth mentioning these studies were performed in static conditions, whereas there is a lack of data on the resistance of bimetal components under fatigue. Previous research has presented some fatigue characterizations of (plain) additively manufactured MS1 [21–23] and conventionally fabricated HWS [24]. Leveraging these results, Ebrahimi and Mohammadi [25] have proposed a numerical model to estimate the fatigue life of HAM-produced parts. Nevertheless, this model has yet to undergo experimental validation.

To address this gap in knowledge regarding the fatigue properties of HAM-produced parts, this study presents the results of an experimental campaign. The investigation focuses on hybrid specimens where LPBF is used to fabricate MS1 on top of wrought H11 HWS.

2 | Materials and Methods

Specimen production according to hybrid additive manufacturing was an important challenge in this research. First, a tool steel, namely HWS 1.2343, or X37CrMoV5-1, was used to manufacture a substrate using conventional subtractive techniques. The main applications of this steel involve molds for die casting, tools to be used in aluminum extrusion, extrusion dies, molding plates and inserts for plastic injection mold tools. This material has been selected because hybrid manufacturing opens many possibilities in the field of rapid tooling, where additive manufacturing may be used for repair purposes or for basement upgrading with simultaneous fabrication of cooling channels. In particular, the stacking fabrication of a monolithic upper part containing cavities prevents expensive and time-consuming additional subtractive machining. The ultimate tensile strength (UTS) and yield strength (YS) of this material may be increased to 1650 and 1500 MPa, respectively, after a proper heat treatment, which entails a hardness rise to 50 HRC. This treatment consists of three-step heating to the 1010 to 1040 °C austenitization temperature (a first preheating at 620 °C, a second one at 830 °C, and the last one at the austenitization temperature), with subsequent fast cooling (quenching) in oil or pressurized gas to the temperature of 530 °C, a double tempering at a temperature between 200 and 400 °C, and final air cooling to the room temperature. The composition of this steel, as weight percentage, is provided in Table 1, according to [26, 27]. The same tool steel was then utilized to manufacture 17 samples with cylindrical shape and 12 mm diameter. Conventional subtractive techniques were again utilized for this purpose, thus producing 80-mm-high cylinders to be then upgraded by additive manufacturing.

As a further step, an approximately 20-mm-long thread was cut at one hand of each cylinder, while a threaded hole was drilled at the baseplate. Threaded coupling made it possible to fix the 17 cylinders to the baseplate in their vertical position, i.e., with their axis being perpendicular to the baseplate. Once assembled, the 17 cylinders were ground in order to have their top surfaces lying on the same plane. Afterward, LPBF, in particular, direct metal laser sintering (DMLS) technology was used to extend the cylinders. Maraging steel MS1 (18% Ni Maraging 300 or AISI 18Ni300) powder was utilized for this purpose. This material has several applications in the automotive and in the die industry. Moreover, it is particularly suitable for hybrid manufacturing and repair purposes, as highlighted in [18–20]. Its chemical composition is also reported in Table 1.

As for static mechanical properties, a UTS of 2050 MPa and a YS of 1990 MPa can be achieved following a proper heat treatment that leads to a hardening of around 50 HRC. Moreover, the fatigue response of additively manufactured maraging steel is also well known based on previously published results by the present research group [21, 23, 28, 29]. The 17 samples were upgraded with cylindrical shapes with the same 12 mm diameter by an additional 60 mm to a final overall length of approximately 120 mm, excluding the threaded part connected to the baseplate (140 mm including the threaded part). The specimens were manufactured by EOSINT M280 system (EOS GmbH - Electro Optical Systems, Krailling/Munich, Germany), equipped with Ytterbium fiber laser with 200 W power and emitting 1064 nm wavelength infrared light beam with 0.2032 mm laser spot diameter. The process was performed in a nitrogen inert environment in a working space with 250 × 250 mm dimensions on the horizontal plane and a maximum height of 325 mm. The layer thickness was set to 40 μm, and a parallel scan strategy with alternating scan direction was adopted. This direction was rotated by 70° at every layer, to get a better structure uniformity. Moreover, a contour line was scanned at every layer to better define the external shape.

The production strategy is sketched in the scheme in Figure 1a. Aging heat treatment was then applied according to the recommendations by the MS1 powder manufacturer [30]: the temperature was increased to 490 °C in 1-h time in an oven. Then, it was held constant for the following 6 h before final gradual cooling in fresh air. Thus, it is worth highlighting that heat treatment was optimized for the additively processed maraging steel MS1.

As a further step, the cylinders were cut as in the sketch in Figure 1a so that the joint between the parts made of 1.2343 steel and MS1 steel was placed in the middle of the sample. Afterward, machining by grinding was run to finally obtain the shape recommended by ISO 1143 standard [31] and displayed in Figure 1b.

Considering the initial 12 mm diameter for the cylindrical shape, allowances of respectively 1 and 3 mm could be achieved at the heads (having a 10 mm diameter) and at the gage (6 mm diameter). These allowance levels are consistent with the normally used ones and the results in [21, 29].

Sample finishing was completed by shot-peening using stainless steel spherical shots with 400 μm diameter under a flow pressure of 5 bar. A collection of samples is displayed Figure 1c, where the additively processed side is on the left.

3 | Experimental

Before starting experimental testing, dimensional and roughness measurements, both at gages and at the heads, were performed on all the samples. Measurements were replicated at least six times for the sake of statistical evidence. All the samples appeared to be compliant with dimensional specifications and tolerance ranges as well as roughness values according to Standard ISO 1143 [31].

Rockwell hardness measurements were carried out, running 6 measurements per sample and, therefore, 102 measurements as a total. Measurements were run, considering 120° equally spaced spots on both the specimen heads, corresponding to the two materials connected. This analysis was important in order to compare the retrieved hardness values to the expected static strengths for additively processed MS1 and wrought HWS and the observed fatigue response. The plain experimental hardness yields were then corrected complying with Standard [32] to take the actual convex surface curvature and its relatively small radius into account. Average values were finally computed.

TABLE 1 | Chemical composition (weight percentage) of HWS 1.2343 (X37CrMoV5-1) and maraging steel MS1.

HWS 1.2343 (X37CrMoV5-1)

C [%]	P [%]	S [%]	Si [%]	Mn [%]	Cr [%]	Mo [%]	V [%]	Fe [%]
0.33–0.41	≤ 0.02	≤ 0.03	0.80–1.20	0.25–0.50	4.80–5.50	1.10–1.50	0.30–0.50	Bal.

Maraging steel MS1

Ni [%]	Co [%]	Mo [%]	Ti [%]	Al [%]	Cr [%]	Cu [%]	C [%]	Mn [%]	Si [%]	P [%]	S [%]	Fe [%]
17–19	8.5–9.5	4.5–5.2	0.6–0.8	0.05–0.15	≤ 0.5	≤ 0.5	≤ 0.03	≤ 0.1	≤ 0.1	≤ 0.01	≤ 0.01	Bal.

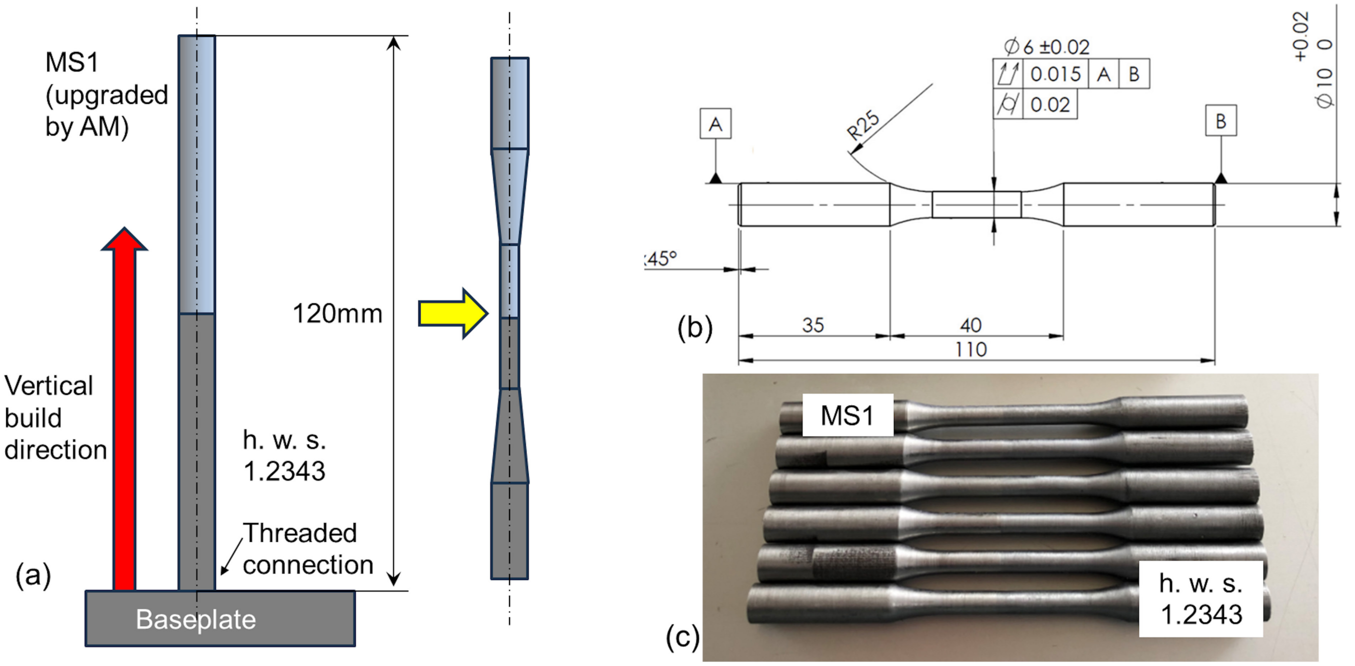

FIGURE 1 | (a) A scheme of hybrid additively manufactured sample preparation. (b) Sample for fatigue tests under rotary bending (all dimensions in mm). (c) Some of the samples after fabrication (additively processed side on the left). [Colour figure can be viewed at wileyonlinelibrary.com]

Fatigue testing was performed by rotary bending using an electrically actuated machine (RB 35, by Italsigma, Forlì, Italy). This machine operates under load control, and loads were applied in a four-point bending configuration, so that the entire specimen and, in particular, its gage operate under a constant maximum moment. Fatigue cycling was conducted by a fully symmetric tension-compression loop with stress ratio $R=-1$ at the frequency $f=60\,\text{Hz}$. Maximum bending moment was controlled throughout every entire trial by a closed-loop control device, so that, based on the set bending moment, the maximum bending stress acting at gage was also controlled. The stress levels for each test are provided in the "Results and Discussion" section. The failure criterion was breakage consisting of specimen separation, which triggered the machine to stop. A 10 million cycles runout value was set, based on recommendations in previous studies dealing with additively manufactured Maraging steel MS1 under fatigue [21, 23, 28, 29]. The results were processed to determine the S-N curve in the finite life domain and the fatigue limit for infinite life. The S-N curve was initially processed by a linear and quadratic regression, as recommended in Standard ISO 12107 [33]. Afterward, the general linear test was applied to assess if the improvement achievable by the more sophisticated quadratic model was significant with respect to the more conventional linear model The analysis was completed by the determination of confidence bounds for 10 and 90% probabilities of failure and 90% confidence level. A possible limitation of this conventional approach is that failure data only can be considered for determining the curve by interpolation. Therefore, a "Maximum Likelihood Estimation (MLE)" approach was also applied. This procedure enables the determination of S-N curve trends, accounting not only for failure data (the so-called complete data), but also for runout outcomes (censoring data). Consequently, both the sloping part of the Wohler curve and the nearly horizontal part in the neighborhood of the fatigue limit can be accurately modeled. These two parts composing the curve are suitably filleted. This method was initially developed by [34] and is based on the maximization of the logarithm of a likelihood function, which leads to a more accurate determination of the S-N curve [35–37].

This procedure has led to the determination of stress-lifecycles curves, involving both the sloping part (for high stress levels) and the fatigue limit for infinite life. As above, this methodology arises from the implementation of the likelihood function L that is provided in Equation (1). An optimization approach aimed at the maximization of the logarithm of this likelihood function, as in Equation (2), is then pursued. This procedure takes advantage of the monotonic trend of the logarithm function and its basic property of turning products into sums. This feature facilitates the optimization algorithm and leads to more efficient and accurate iterative computation.

$$L=\prod_{i=1}^{n}\left\{\phi\left(\frac{Log(N_i)-\left(b_0+b_1\cdot Log(S_i)\right)}{\sigma_{Log(N)}}\right)^{\delta_i}\Phi\left(\frac{S_i-\mu_S}{\sigma_S}\right)^{\delta_i}\left[1-\Phi\left(\frac{Log(N_i)-\left(b_0+b_1\cdot Log(S_i)\right)}{\sigma_{Log(N)}}\right)\Phi\left(\frac{S_i-\mu_S}{\sigma_S}\right)\right]^{1-\delta_i}\right\} \tag{1}$$

$$ln(L)=\sum_{i=1}^{n}ln\left\{\phi\left(\frac{Log(N_i)-\left(b_0+b_1\cdot Log(S_i)\right)}{\sigma_{Log(N)}}\right)^{\delta_i}\Phi\left(\frac{S_i-\mu_S}{\sigma_S}\right)^{\delta_i}\left[1-\Phi\left(\frac{Log(N_i)-\left(b_0+b_1\cdot Log(S_i)\right)}{\sigma_{Log(N)}}\right)\Phi\left(\frac{S_i-\mu_S}{\sigma_S}\right)\right]^{1-\delta_i}\right\} \tag{2}$$

In these formulas, N_i are the observed lives for tests under rotary bending with stress ratio $R = -1$, under the amplitude S_i (which corresponds to maximum bending stress). It is supposed that lifespan exhibits a log-normal distribution with standard deviation $\sigma_{\text{Log(N)}}$ and a mean value corresponding to the life prediction according to the S-N curve, and that the stress at the fatigue limit has a Gaussian Distribution with mean value μ_S and standard deviation σ_S. Regarding these assumptions, Φ indicates the cumulative distribution function of the Normal distribution. Conversely, ϕ refers to the probability density function of the same distribution. Finally, δ_i is a discrete parameter assuming the values 1 and 0 for respectively failure (complete, not censoring) and runout (censoring) data. Finally, n refers to the overall number of conducted trials, regardless their failure or not-failure outcomes.

$$p = \Phi\left(\frac{Log(\overline{N}) - (b_0 + b_1 \cdot Log(\overline{S}))}{\sigma_{Log(N)}}\right) \cdot \Phi\left(\frac{\overline{S} - \mu_S}{\sigma_S}\right) \tag{3}$$

The fatigue curve has been determined, considering that the probability of failure p for a set stress $\overline{S}$, after N cycles, is yielded by Equation (3). Therefore, this equation can be inverted, in order to determine the expected lifespan, based on different values for the applied stress. This procedure has initially been applied for a probability of failure of 50%. Subsequently, lower and upper bounds corresponding to failure probabilities p of 10% and 90%, respectively, have been determined as well. The fatigue limits were determined based on the failure-not-failure sequences, in agreement with the Dixon method, i.e. an abbreviated staircase procedure involving 8 to 10 nominal samples [38–42]. Fatigue limit confidence bands at the 90% confidence level, taking both data scattering (variance) and the number of nominal samples (sequence size) into account, were determined as well.

Micrographic studies were run to assess the layered structure arising from the additive process at the interface with the wrought material where the upgrade process was started. For this purpose, resin-embedded samples underwent chemical etching according to two procedures by Fry for 80 s and Vilella for 10 min without heating. Afterward, samples were dried with compressed air. Observations of resin-embedded samples were carried out by an optical microscope (Optiphot-100, by Nikon, Melville, NY, United States).

The same embedded samples, before chemical etching, were used for porosity analysis. Where porosities are not present, the investigated area appears black. The presence of porosities entails a different light reflection, which results in voids appearing bright and shining under a light source. The images recorded by a stereo-microscope (Stemi 305, by ZEISS, Oberkochen, Germany) were processed by converting the RGB to layers, then binarizing the image to convert bright and dark tones to white and black, respectively; then, converting colors into grayscale and reversing the colors. In these conditions, voids and porosities are made clearly visible, as they exhibit dark shadows over a clear landscape: The amount of black with respect to white may be easily computed by several freeware software. As a final step, the ratio between the black and the white pixels yields the porosity level of the specimen concerning the analyzed area.

Fracture surfaces have been analyzed with the aid of the aforementioned stereo-microscope, aiming to individuate the crack nucleation sites and triggers, as well as crack propagation paths up to final failure. As a further step, the fractographic study was completed by a hot-cathode field emission gun (FEG) scanning electron microscope (SEM) that is equipped with secondary electron detector, wobble adjustment and stigmator alignment for high-resolution imaging (Mira3 Model, by TESCAN, Brno, Czech Republic). This tool provided an important contribution to the individuation of the primary sources for cracking, with reference to the joint, the wrought material and the additively manufactured one. Its essential role was also focused on the investigation regarding the fracture mode (brittle vs. ductile), depending on material properties. This investigation was based on the observation of both propagation striations and final fracture morphologies.

4 | Results and Discussion

The results of the fatigue tests are collected in Table 2, where data regarding the controlled stress level, the observed lifespan, the final outcome, and the fracture location are provided. With reference to the latter, W indicates the crack started from the wrought material, whereas A indicates initiation at the additively processed MS1. Finally, M is related to separation occurring in the middle, i.e., at the joint between the two materials.

TABLE 2 | Recorded fatigue data.

Stress (MPa)	Lifespan (cycles)	Outcome (failure/runout)	Failure location (A/M/W)
490	4888	Failure	M
400	49,863	Failure	M
400	29,761	Failure	W
310	381,642	Failure	M
250	7,167,421	Failure	A
230	10^7	Runout	
250	10^7	Runout	
270	10^7	Runout	
290	375,459	Failure	W
270	732,423	Failure	W
250	10^7	Runout	
310	1,410,982	Failure	A
340	109,620	Failure	M
340	257,165	Failure	M
370	37,800	Failure	M
370	90,125	Failure	M
290	903,232	Failure	A

Data have been processed for the determination of the S-N curve in the finite life domain complying with ISO [33]. In particular, they have been interpolated by a linear model, according to Equation (4), for which the following coefficients apply: $b_0 = 30.229$, $b_1 = -9.873$, $k{\cdot}\sigma = 0.531$.

$$Log(N) = b_0 + b_1 \cdot Log(S) \pm k \cdot \sigma \quad (4)$$

As recommended by Standard and as highlighted above, data were also interpolated through a quadratic model, but the general linear test (GLT) confirmed that the achievable improvement is not significant. The curve is plotted in Figure 2a for life cycles ranging between 10^4 and 10^7 cycles together with its lower and upper bounds corresponding to, respectively, 10% and 90% failure probability for a 90% confidence level. The width of the scatter band is related to the term $k{\cdot}\sigma = 0.531$, which is also included in the S-N equation. In addition, the scatter index T_σ has been computed as the ratio between the fatigue strengths corresponding to $N = 10^7$ cycles (runout) for respectively 90% and 10% probabilities of failure. Experimental data are plotted as well (except for the first one, tested at the highest load of 490 MPa), and runouts are highlighted by right-bound arrows.

As mentioned in the previous section, the same data were also processed by the MLE, which made it possible to take not only complete but also censoring data (i.e., runouts) into account.

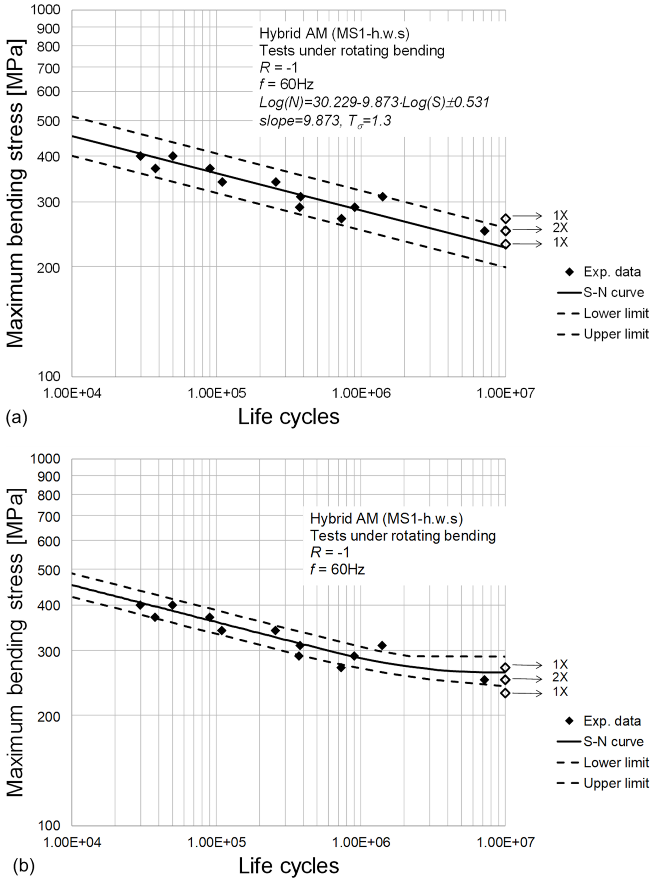

FIGURE 2 | (a) S-N curve in the finite life domain according to ISO 12107 [33]. (b) S-N curve and fatigue limit complying with an MLE approach [34]. [Colour figure can be viewed at wileyonlinelibrary.com]

The curve determined through the maximization of the maximum likelihood function is plotted in Figure 2b, again with its confidence band, whose lower and upper bounds are related to 10% and 90% failure probabilities, as stated above. The fatigue response can be compared to that observed for (completely) additively manufactured maraging steel MS1. Its determination was the topic of a previous study by the same group, whose results are available in [29]. It is worth mentioning that this previous study involved samples of the same material of the additively processed regions, which underwent the same fabrication process as well as the same post-manufacturing surface and heat-treatments, including final shot-peening. In addition, all of the steps of the production process were followed, according to the same order, as described in the present study. Thus, the retrieved fatigue curve in [29] is plotted in Figure 3a together with the here determined curve.

The same processing method (MLE) is adopted here for the sake of consistency upon curve comparison. It is clear that the fatigue strength (for both finite and infinite life) is sharply dropped down (approximately reduced to one-half) for hybrid additively manufactured MS1, as it is combined with tool steel. A similar conclusion can be drawn if fatigue limits, here estimated as fatigue strengths at runout, are compared. These strengths, estimated by the tool of the Dixon abbreviated staircase, are provided in the bar graph in Figure 3b.

Based on the aforementioned results, it is clear that the fatigue response of hybrid additively manufactured MS1 is

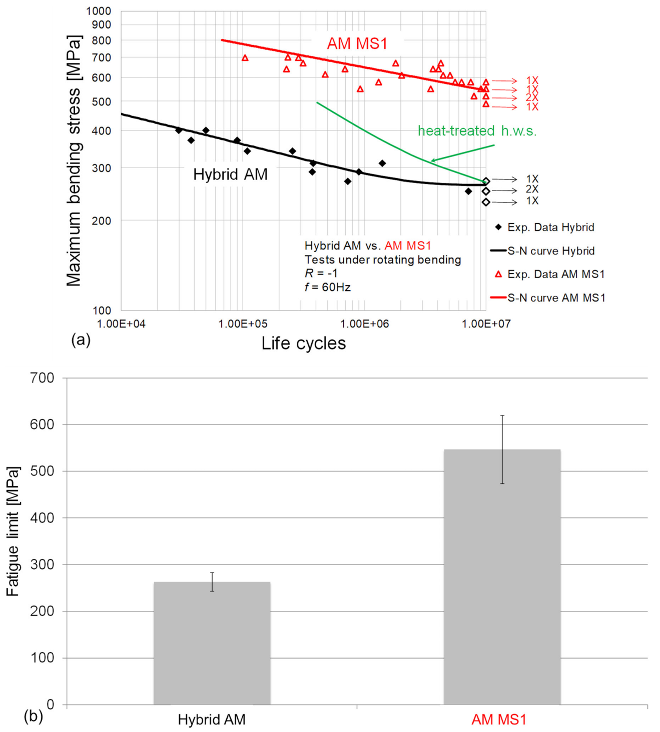

FIGURE 3 | (a) Comparison of fatigue curves for Hybrid additively manufactured MS1, for additively processed MS1 and for HWS wrought material. (b) Fatigue strengths at runout (10^7 cycles) for hybrid additively manufactured MS1 and for additively processed MS1 (same heat- and surface-treatments). [Colour figure can be viewed at wileyonlinelibrary.com]

much lower than that of the plain additively processed MS1. Thus, the focus was moved to the wrought material counterpart, i.e., 1.2343 hot-working tool steel. Regarding the latter, a fatigue characterization of this material, following proper heat treatment, as described in the "Materials and Methods" section, was run in [26] under tension-compression axial load by a servo-hydraulic machine. Fatigue trials were conducted under stress-controlled condition, accounting for 4 stress levels. The retrieved curve is plotted together with the other ones in Figure 3a for comparison purposes. It can be remarked the fatigue strength of the heat-treated HWS is again higher than the observed one for the hybrid produced samples. Possible reasons may rely on (i) the joint between MS1 and HWS acting as a weak point that is likely to trigger the failure of the additively processed part; (ii) the heat-treatment being here optimized for MS1 (in particular, performed, according to the recommendations from the powder supplier) and not for HWS. The latter occurrence could be expected to lead to a reduced performance of the HWS. Thus, the following subsections are devoted to the investigations and the experimental analyses performed in order to address these two points.

4.1 | Micrographies and Porosity Analyses

As a first step, the joint between the additively processed part and the HWS acting as a wrought material substrate has been observed, following plain polishing without any additional chemical etching. The picture shown in Figure 4a has been taken by a stereoscopic microscope, and tags are added to highlight the wrought material (HWS) and the additively manufactured one upon the upgrade procedure (MS1). A detail is displayed in Figure 4b: This picture, captured by an optical microscope, clearly highlights the joint between the two materials and the stacked structure of the deposited material.

As described above, these images have been turned into gray scales. Following color inversion, they have been processed by graphic software to work out the level of porosities (area of black regions over white regions) and the estimated relative density (as a complement of 100%). The basic hypothesis was that the porosity level of the additively processed material was likely to be significantly incremented in the neighborhood of the joint between the two materials. This result is in line with the findings by Azizi et al. [18], who highlighted a considerable porosity at

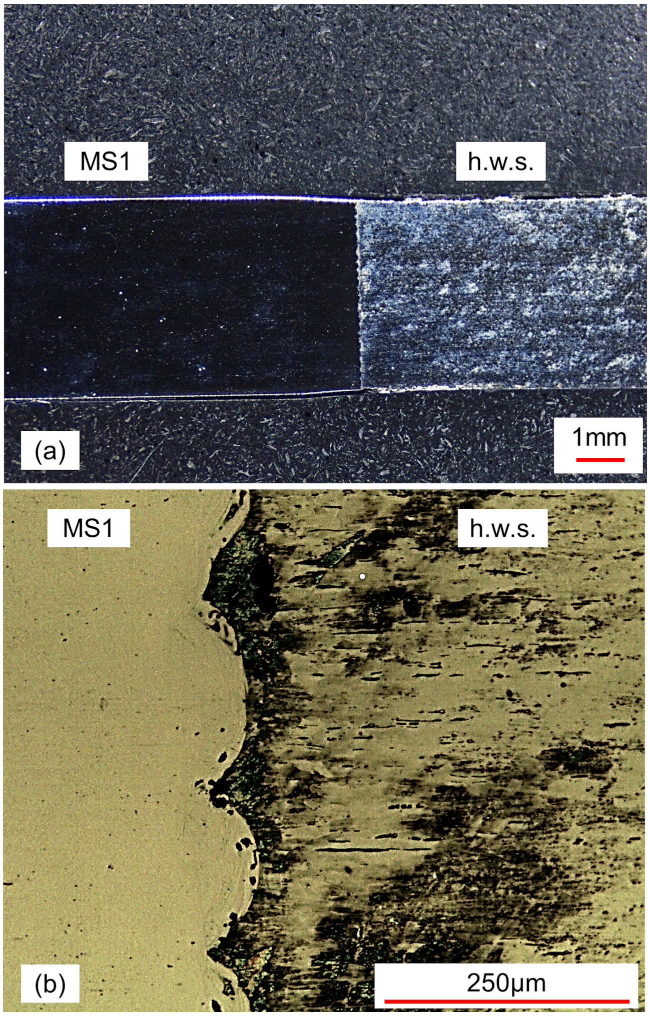

FIGURE 4 | (a) Stereoscopic microscope view at the joint between MS1 and HWS. (b) Detail by optical microscope. [Colour figure can be viewed at wileyonlinelibrary.com]

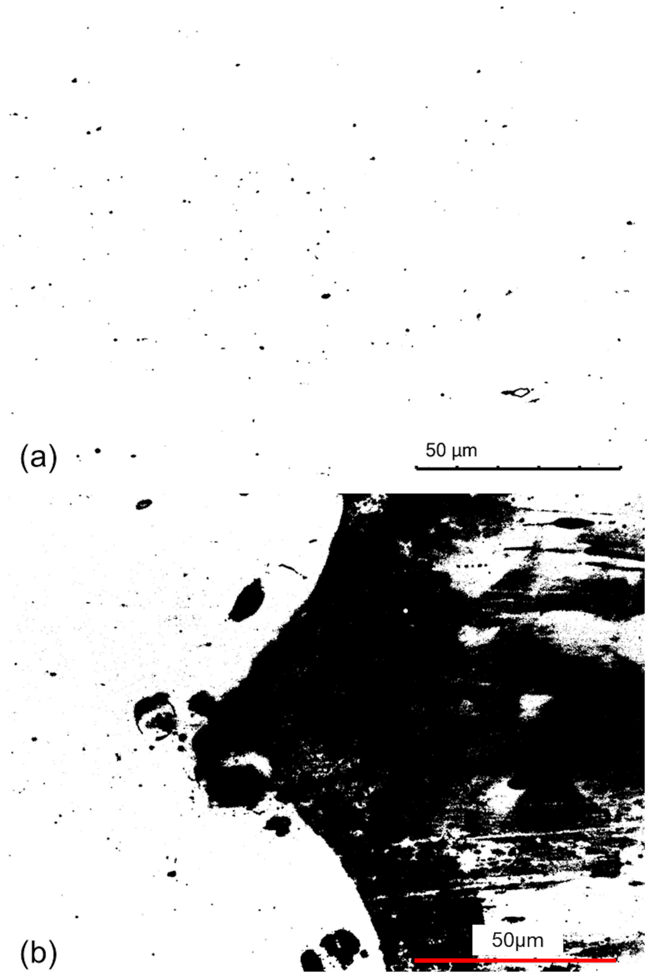

FIGURE 5 | Porosities (highlighted by dark pixels over a white background) in the additively manufactured MS1 (a) far away from the joint and (b) close to the joint between the additively manufactured MS1 (left side) and the HWS (right side). [Colour figure can be viewed at wileyonlinelibrary.com]

the joint region. Thus, the analysis was initially focused on some areas far away from the joint, in order to have a term of comparison. Afterward, it was moved to the transition between the wrought material substrate and the additively processed MS1. The outcome of the first analysis is shown in Figure 5a (measurements have been run over different spots, computing then an average).

It can be pointed out the average level of porosity is 0.2% (ranging from a minimum of 0.1% to a maximum of 0.3%), corresponding to an average relative density of 99.8% (from a minimum of 99.7% to a maximum of 99.9%), which is absolutely consistent with that of a properly fabricated MS1, following a regular stacking process [30]. Conversely, in the neighborhood of the joint, the porosity level is sharply incremented by one order of magnitude to an average of 2.3% (ranging from a minimum of 1.8% to a maximum of 4.2%), corresponding to an average relative density of 97.7% (from a minimum of 95.8% to a maximum of 98.2%). In this case, measurements over different spots have also been conducted, provided that the largest black shadows, which may have biased the analysis, have been disregarded. The processed micrography is provided in Figure 5b. Therefore, as a matter of fact, the retrieved data confirm that the joint appears as a weak point, which, in turn, is related to a significant increment of voids.

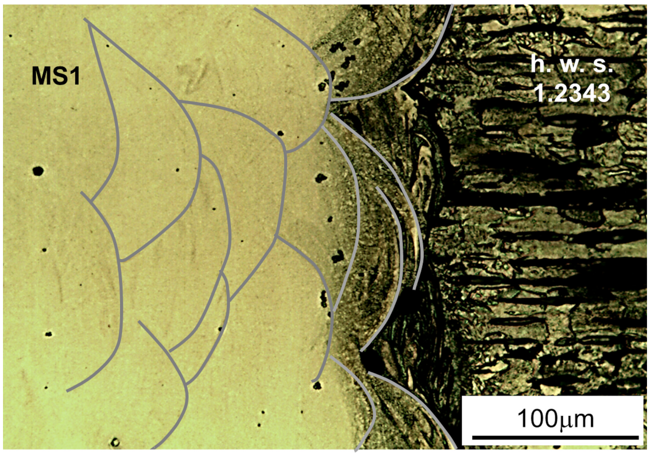

FIGURE 6 | Joint between HWS and the stacked structure of the additively fabricated MS1. [Colour figure can be viewed at wileyonlinelibrary.com]

Moreover, as highlighted in [43], a possible reason for weakness and defects at the interface between the two materials could be the elemental segregation at the grain boundaries in the transition. This kind of segregation, often involving Cr and Mo, has been found to be a driving force for the generation and propagation of cracks that typically initiate from voids and porosities due to lack of fusion [44]. This phenomenon, entailing a strong relationship between segregation, the occurrence of defects, and consequent weakness, was also observed in other studies, such as [45] and [46]. In particular, the relevant role of segregation in intermetallic phases is emphasized in the latter as segregated phases are frequent crack initiation sites and may affect crack propagation paths under the additive process-induced residual stresses.

The analysis has then been completed, running chemical etching and re-observing the sample. The related image (Figure 6) again clearly shows the joint between the two materials, while the stacked structure arising from the additive fabrication is also quite evident and here highlighted by graphical post-processing.

4.2 | Hardness Measurements

As a first step, HRC hardness was measured on both sides. However, the values for the wrought material were too low and laid out of the HRC scale (under its minimum threshold), which would have prevented a direct comparison to

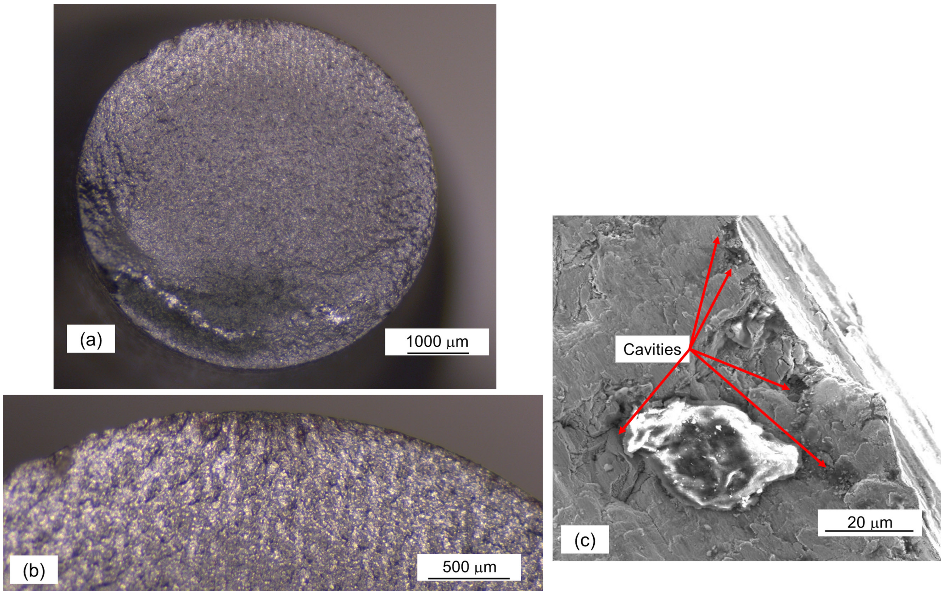

FIGURE 7 | (a) General view of the fracture of a sample that failed in the additively processed part. (b,c) Details of crack initiation from subsurface defects. [Colour figure can be viewed at wileyonlinelibrary.com]

the hardness of the wrought material side. Therefore, HRA measurements (by a conical penetrator, 588 N) were run for both sides. The rationale was taking advantage of the larger range covered by the HRA scale so that the same scale could be used for both sides, which enabled direct comparisons between the achieved hardness for additively processed MS1

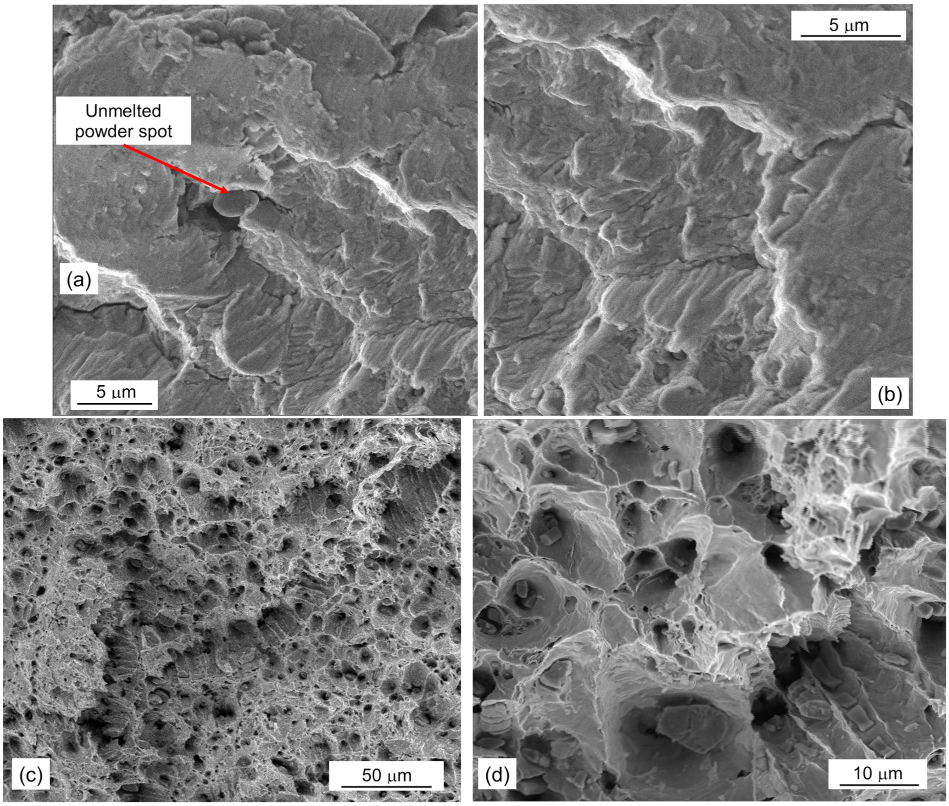

FIGURE 8 | (a,b) Details of propagation in the additively processed part. (c) Final fracture in the additively processed part following a ductile mechanism. (d) Detail of dimples. [Colour figure can be viewed at wileyonlinelibrary.com]

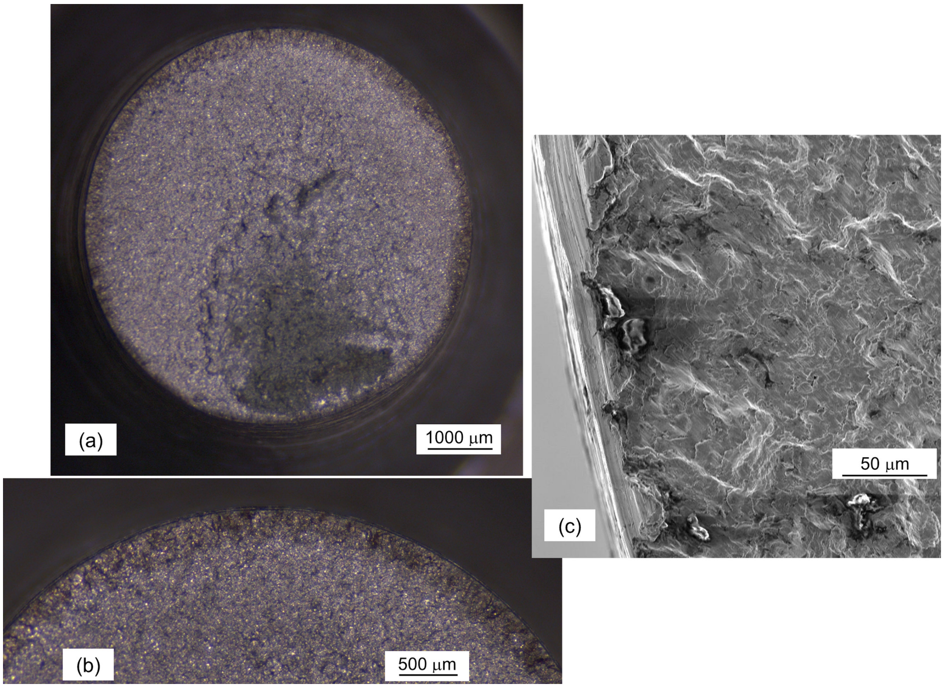

FIGURE 9 | (a) General view of the fracture of a sample that failed in the wrought material part. (b,c) Details of crack initiation from surface defects. [Colour figure can be viewed at wileyonlinelibrary.com]

and HWS, as results of fabrication and post-fabrication processes. Regarding additively processed MS1, hardness was ranging between 77.1 and 79.3 HRA, with a mean value around 78 HRA corresponding to around 54 HRC. This outcome is fully consistent with the expected values as a result of the aging treatment recommended by the powder supplier [30]. Conversely, hardness at the opposite side for HWS was dramatically lower: between 54.1 HRA and 55.8 HRA, which leads to a mean value of 55HRA, corresponding to just 8 HRC. This outcome is presumably due to not proper and [30] not optimized heat-treatment for the HWS and is consistent with the mechanical properties of the not treated material. The recommended treatment for HWS would have required hardening up to the austenitization temperature of 1010–1040 °C,

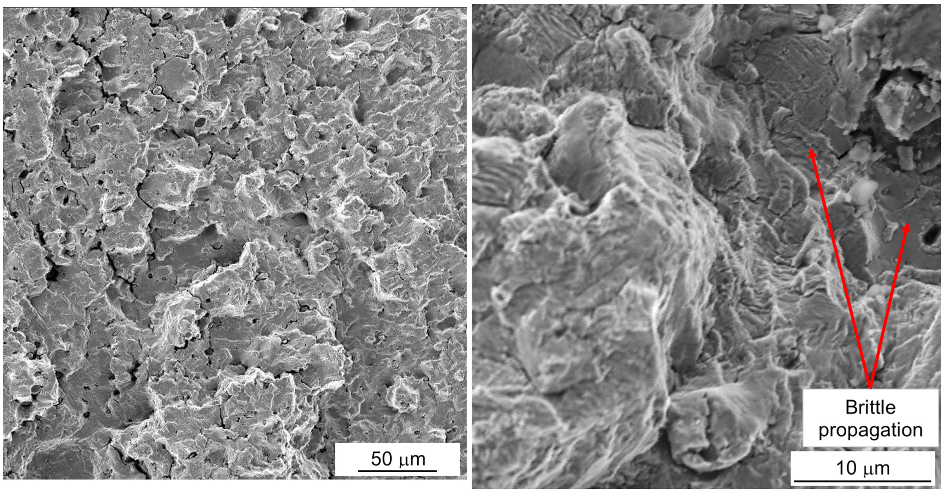

FIGURE 10 | (a) Final fracture following a brittle mechanism in the HWS and (b) a detail of propagation. [Colour figure can be viewed at wileyonlinelibrary.com]

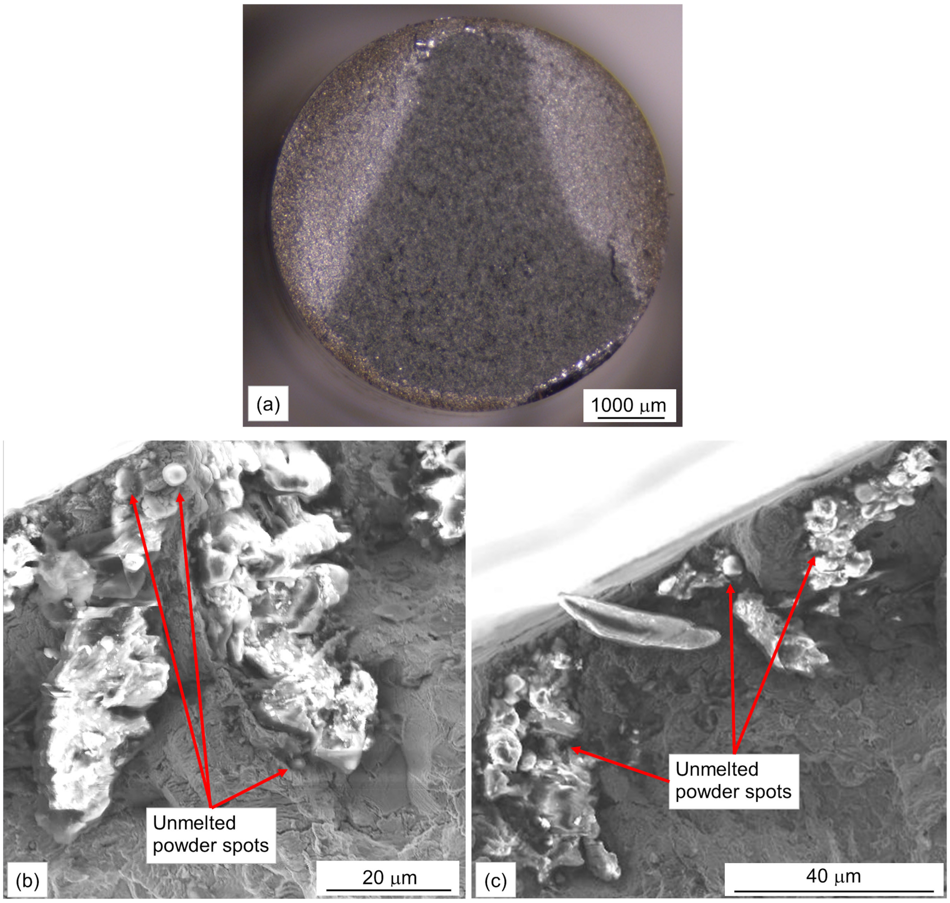

FIGURE 11 | (a) Fracture surface at the interface between the additively processed and the wrought material. (b) Some details of initiation points at the joint. Unmelted powder spots being responsible for cavities and incremented porosity at the interface are also visible. [Colour figure can be viewed at wileyonlinelibrary.com]

quenching in oil and subsequent double tempering. However, this temperature would not have been tolerated by MS1, because it would have caused a loss in strength due to precipitate coarsening and decomposition of the martensite with a reversion back to austenite.

The treatment for MS1 was followed, instead, by aging at 490 °C. Therefore, austenitization of HWS could not take place, and, as a consequence, conversion to Martensite was also prevented.

The problem of very different heat treatment procedures is still an issue for depositing maraging steel powder on top of conventionally fabricated tool steels. As highlighted in [19], in bi-metallic components, the unique heat treatment needs to be optimized for one of the two materials, which may lead to a lower resistance than expected for the other material. For certain specific combinations, it is feasible to execute the optimal heat treatments of the two materials sequentially, thereby attaining superior properties in the resultant joint [20]. However, generally, the heat treatment requires a compromise to avoid an excessive penalization in the properties of one of the two materials involved in the joint [22]. This is especially true in the case of hybrid joints between HWS and maraging steel, since these materials ideally require significantly different treatments [19].

4.3 | Fracture Surface Analyses

Fractographic analyses have been run on the specimens, accounting for cases where cracks started from the additively manufactured MS1, the wrought tool steel, and at the joint between them. Thus, according to the details provided in Table 2, the fracture surfaces of specimens within these categories have been investigated. The image in Figure 7a,b refers to the fracture observed in a sample where failure initiated from MS1. This picture, taken by a stereoscopic microscope, refers to the overall fracture surface.

The analysis was then deepened by SEM-FEG observation with the purpose of addressing the primary reason that promoted crack initiation and subsequent propagation. The detail of initiation displayed in Figure 7c indicates that cracks started from voids and porosities just beneath the external surface. In particular, cavities at the depth of some tenths of μm from the external surface are present. This mechanism of crack nucleation is consistent with that described in several papers, such as [28, 29], dealing with the fatigue response of additively processed MS1. With reference to subsequent propagation, it proceeded regularly with equally sized and spaced striation marks, as highlighted in Figure 8a,b. The focus was then moved to the final fracture area, in order to investigate the predominant fracture mode. The image displayed in Figure 8c,d reveals that failure must be regarded as ductile, as highlighted by the clearly visible dimples.

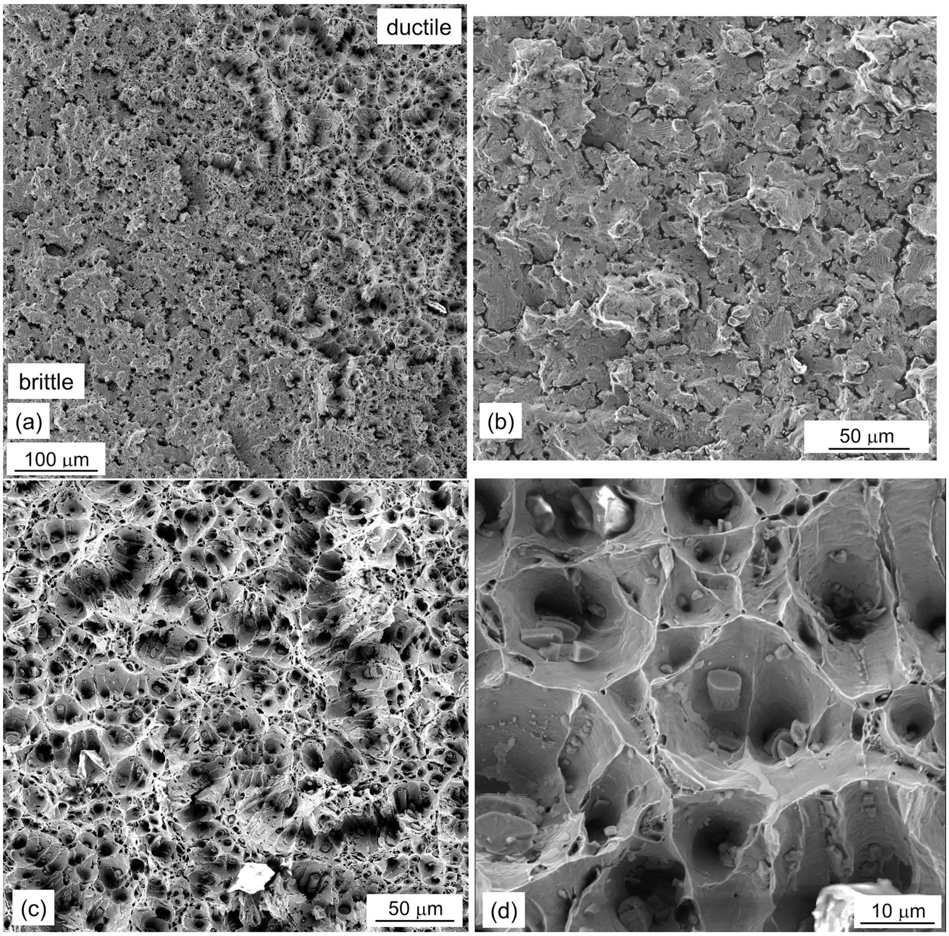

FIGURE 12 | Final fracture at the interface between the additively processed (MS1) and the wrought (HWS) material. Details of the (b) brittle fracture and the (c,d) ductile failure mode. [Colour figure can be viewed at wileyonlinelibrary.com]

The following step regarded investigating a failure that started from the HWS. In this case also, the overall fracture surface, which is visible in Figure 9a,b (picture taken by stereoscopic microscope), was further investigated by SEM-FEG. As highlighted in Figure 9c, initiation is, in this case, triggered by some surface defects. The final fracture exhibits a completely different failure mode with respect to that of the additively manufactured MS1. In particular, the failure mechanism is turned from ductile to brittle, which can be regarded as a further significantly detrimental effect introduced by the not properly heat-treated HWS. An example of brittle fracture mode is displayed in Figure 10a. As a consequence of the prevalent brittle mode, striation marks are not clearly visible. An example is shown in Figure 10b, where some close striations are present on its left side, and a perpendicular flaw with a further fracture on a parallel plane is also visible. The latter, on the right side of the picture, must be regarded as a purely brittle fracture: In this case, no striations can be observed despite the high magnification.

As previously highlighted, failure mainly occurred at the joint between the additively manufactured and the wrought material. An example of a complete fracture surface is shown in Figure 11a. Detailed observations by SEM-FEG indicated that failure was generally promoted by the increased number of porosities at the interface between the two materials, as highlighted in the “Discussion” section. An example of an initiation point is shown in Figure 11b,c, where voids, as well as unmelted powder spots, are visible. Final breakage generally involves the two materials. It is interesting to highlight that a ductile failure mechanism can be spotted with reference to the MS1, whereas a brittle mode is again revealed for the portion made of HWS. It is worth mentioning that a transition at the interface between the two materials is clearly visible in Figure 12a, where the two parts are tagged for the sake of clarity. Details regarding both the brittle and the ductile propagations, for respectively the HSW, and the additively manufactured MS1, are provided in Figure 12b–d. A brittle behavior for the HWS portion, as highlighted in Figure 10b, can therefore be identified as a further relevant reason for premature failure of the here studied specimens under fatigue with respect to these completely fabricated by additively processed MS1.

On the whole, the following remarks may be made to explain fracture in the three described scenarios.

As highlighted in Table 2, most specimens failed at the joint between the two materials with initiation from porosities at MS1 part. The primary reason for these premature failures with respect to completely additively processed MS1 is related to the sharply incremented porosity at the interface between the two materials. The brittle behavior of the HWS also promoted rapid propagation to final failure. In addition, a not negligible number of samples experienced failures with initiation, propagation and final breakage involving only the HWS portion. In this case, the brittle fracture mechanism was prevalent to lead parts to premature failure. Finally, a lower amount of samples experienced failures that started from the MS1 counterpart with consequent propagation and final separation through this material. In this case, failure occurred consistently with [28, 29] and was promoted by sub-surface porosities that are usually present in stacked material and are often due to lack of penetration of the molting pool. Ductile propagation with visible striation marks up to final failure with clearly visible dimples occurred at the following stages.

5 | Conclusions

This experimental study has investigated the fatigue response of a Hot Work Steel (1.2343) part, when it is upgraded by the stacking deposition of Maraging steel MS1, applied by laser powder bed fusion. The recommended heat-treatment for MS1 has also been performed before final shot-peening.

The most interesting findings are reported in the points below.

- Rotary bending fatigue test results have returned a fatigue strength of approximately one-half of that for the completely additively fabricated MS1 (the here observed fatigue limit for infinite life is 260 MPa vs. around 550 MPa for MS1).
- Microscopy observations at the joint between the two materials have revealed that the porosity level of the additively processed part is remarkably incremented by a factor of 30 (from 0.1 to 3.2%) with respect to its conventional level when measured far away from the joint. This outcome proves the interface between the two materials is indeed a weak point.
- Hardness proved to be dramatically lower on the hot work steel side due to the conducted heat treatment optimized for the maraging but not for the hot work steel. A higher temperature level would have been needed for the hot work steel, but could not have been tolerated by the maraging steel. Finding a good trade-off between the different heat treatments required by the two connected materials is a serious issue.
- SEM observations have finally revealed that the failure mode is brittle in the hot work steel part, and a transition from ductile to brittle fracture is observed at the joint, where most fractures occurred, and which, indeed, acted as a weak point detrimentally affecting strength.

Nomenclature

AM	Additive manufacturing
CNC	Computer numerical control
DED	Direct energy deposition
FEG	Field emission gun
GLT	General linear test
HAM	Hybrid additive manufacturing
HWS	Hot work steel
LPBF	Laser powder bed fusion
MLE	Maximum likelihood estimation
SEM	Scanning electron microscope
T_σ	Scatter index (S-N curve)
UTS	Ultimate tensile strength
YS	Yield strength

Author Contributions

Dario Croccolo: methodology, formal analysis, data curation, writing – review and editing, supervision, funding acquisition. **Snežana Ćirić-Kostić:** conceptualization, resources, writing – review and editing, supervision, project administration, funding acquisition. **Massimiliano De Agostinis:** validation, formal analysis, data curation, writing – review and editing. **Stefano Fini:** validation, formal analysis, data curation, writing – review and editing. **Mattia Mele:** formal analysis, investigation, data curation, writing – original draft, writing – review and editing, visualization. **Nebojša Bogojević:** conceptualization, resources, data curation, writing – review and editing, project administration. **Vladimir Sinđelić:** resources, data curation, writing – review and editing. **Giorgio Olmi:** methodology, formal analysis, investigation, writing – original draft, writing – review and editing, visualization, supervision, project administration.

Acknowledgments

The research presented in the paper represents a part of research carried out within the project "Advanced design rules for optimal dynamic properties of additive manufacturing products – A_MADAM." This project has received funding from the European Union's Horizon 2020 research and innovation program under the Marie Skłodowska-Curie grant agreement no. 734455: The authors wish to acknowledge the financial support by the European Commission. Open access publishing facilitated by Universita degli Studi di Bologna, as part of the Wiley - CRUI-CARE agreement.

Data Availability Statement

The data that support the findings of this study are available from the corresponding author upon reasonable request.

References

1. S. Pratheesh Kumar, S. Elangovan, R. Mohanraj, and J. R. Ramakrishna, "Review on the Evolution and Technology of State-of-the-Art Metal Additive Manufacturing Processes," *Materials Today Proceedings* 46 (2021): 7907–7920.

2. P. Stavropoulos, P. Foteinopoulos, A. Papacharalampopoulos, and H. Bikas, "Addressing the Challenges for the Industrial Application of Additive Manufacturing: Towards a Hybrid Solution," *International Journal of Light and Materials Manufacturing* 1 (2018): 157–168.

3. M. Merklein, D. Junker, A. Schaub, and F. Neubauer, "Hybrid Additive Manufacturing Technologies - An Analysis Regarding Potentials and Applications," *Physics Procedia* 83 (2016): 549–559.

4. K. Nyamuchiwa, R. Palad, J. Panlican, Y. Tian, and C. Aranas Jr., "Recent Progress in Hybrid Additive Manufacturing of Metallic Materials," *Applied Sciences* 13, no. 13 (2023): 8383, https://doi.org/10.3390/app13148383.

5. V. V. Popov and A. Fleisher, "Hybrid Additive Manufacturing of Steels and Alloys," *Manufacturing Review* 7, no. 7 (2020): 6, https://doi.org/10.1051/mfreview/2020005.

6. A. Vafadar, F. Guzzomi, A. Rassau, and K. Hayward, "Advances in Metal Additive Manufacturing: A Review of Common Processes, Industrial Applications, and Current Challenges," *Applied Sciences* 11 (2021): 1–33.

7. P. Ferro, A. Fabrizi, G. Savio, R. Meneghello, and F. Berto, "Metallurgical Characterization of Co-Cr-Mo Parts Processed by a Hybrid Manufacturing Technology," *Physical Mesomechanics* 25 (2022): 155–167.

8. J. M. Weaver, J. R. Linn, and M. P. Miles, "Interface Joint Strength Between SS316L Wrought Substrate and Powder bed Fusion Built Parts," *Materials* 14 (2021): 3041, https://doi.org/10.3390/ma14113041.

9. O. Dolev, S. Osovski, and A. Shirizly, "Ti-6Al-4V Hybrid Structure Mechanical Properties—Wrought and Additive Manufactured Powder-Bed Material," *Additive Manufacturing* 37 (2021): 37.

10. A. Schaub, B. Ahuja, L. Butzhammer, J. Osterziel, M. Schmidt, and M. Merklein, "Additive Manufacturing of Functional Elements on Sheet Metal," *Physics Procedia* 83 (2016): 797–807.

11. J. Ma, J. Li, Y. Zhang, et al., "Formation Mechanism of Massive Phase in the Heat Affected Zone of Ti-6Al-4V Fabricated by Forging-Additive Hybrid Manufacturing," *Optics and Laser Technology* 157 (2023): 108698.

12. B. Rankouhi, Z. Islam, F. E. Pfefferkorn, and D. J. Thoma, "Characterization of Multi-Material 316L-Hastelloy X Fabricated via Laser Powder-Bed Fusion," *Materials Science and Engineering a* 837 (2022): 142749.

13. U. Kizhakkinan, S. Seetharaman, N. Raghavan, and D. W. Rosen, "Laser Powder Bed Fusion Additive Manufacturing of Maraging Steel: A Review," *Journal of Manufacturing Science and Engineering* 145 (2023): 1–24.

14. C. Tan, K. Zhou, W. Ma, and L. Min, "Interfacial Characteristic and Mechanical Performance of Maraging Steel-Copper Functional Bimetal Produced by Selective Laser Melting Based Hybrid Manufacture," *Materials and Design* 155 (2018): 77–85.

15. L. Kučerová, I. Zetková, Š. Jeníček, and K. Burdová, "Hybrid Parts Produced by Deposition of 18Ni300 Maraging Steel via Selective Laser Melting on Forged and Heat Treated Advanced High Strength Steel," *Additive Manufacturing* 32 (2020): 101108, https://doi.org/10.1016/j.addma.2020.101108.

16. L. Kučerová, I. Zetková, Š. Jeníček, and K. Burdová, "Production of Hybrid Joints by Selective Laser Melting of Maraging Tool Steel 1.2709 on Conventionally Produced Parts of the Same Steel," *Materials (Basel).* 14 (2021): 1–18.

17. L. Kučerová, Š. Jeníček, I. Zetková, and K. Burdová, "Heat Treatment of Bimetals Produced by Selective Laser Melting of MS1 Maraging Steel on Conventionally Produced 42SiCr Martensitic Steel," *Archives of Civil and Mechanical Engineering* 22 (2022): 1–18.

18. H. Azizi, R. Ghiaasiaan, R. Prager, et al., "Metallurgical and Mechanical Assessment of Hybrid Additively-Manufactured Maraging Tool Steels via Selective Laser Melting," *Additive Manufacturing* 27 (2019): 389–397.

19. S. Shakerin, A. Hadadzadeh, B. S. Amirkhiz, S. Shamsdini, J. Li, and M. Mohammadi, "Additive Manufacturing of Maraging Steel-H13 Bimetals Using Laser Powder bed Fusion Technique," *Additive Manufacturing* 29 (2019): 29.

20. S. Shakerin, M. Sanjari, H. Pirgazi, B. S. Amirkhiz, and M. Mohammadi, "On the Bending of MS1-P20 Hybrid Steels Additively Manufactured Using Laser Powder bed Fusion," *Materialia.* 24 (2022): 101501.

21. D. Croccolo, M. De Agostinis, S. Fini, G. Olmi, A. Vranic, and S. Ciric-Kostic, "Influence of the Build Orientation on the Fatigue Strength of EOS Maraging Steel Produced by Additive Metal Machine," *Fatigue and Fracture of Engineering Materials and Structures* 39 (2016): 637–647.

22. G. Meneghetti, D. Rigon, D. Cozzi, W. Waldhauser, and M. Dabalà, "Influence of Build Orientation on Static and Axial Fatigue Properties of Maraging Steel Specimens Produced by Additive Manufacturing," *Procedia Structural Integrity* 7 (2017): 149–157.

23. D. Croccolo, M. De Agostinis, S. Fini, et al., "Sensitivity of Direct Metal Laser Sintering Maraging Steel Fatigue Strength to Build Orientation and Allowance for Machining," *Fatigue and Fracture of Engineering Materials and Structures* 42 (2019): 374–386.

24. J. Zhang, J. Schumacher, and B. Clausen, "A Comprehensive Study on the Influence of the Scan Pattern in Two Porosity Levels and Surface Roughness on the Fatigue Behavior of Laser Powder Bed Fusion Manufactured Specimens Made of Steel H13," *Journal of Materials Science* 58 (2023): 10457–10483.

25. A. Ebrahimi and M. Mohammadi, "Numerical Tools to Investigate Mechanical and Fatigue Properties of Additively Manufactured MS1-H13 Hybrid Steels," *Additive Manufacturing* 23 (2018): 381–393.

26. V. Milovanović, D. Arsić, M. Milutinović, M. Živković, and M. Topalović, "A Comparison Study of Fatigue Behavior of S355J2+N, S690QL and X37CrMoV5-1 Steel," *Metals (Basel)* 12 (2022): 1–14.

27. "Acerol Mittal. 2343 - H11: Hot Work Tool Steel for Die Casting Dies," accessed March 15, 2024. https://preprod-industeel.arcelormittal.com/blog/fichier/ds-tools-2343-h11/.

28. D. Croccolo, M. De Agostinis, S. Fini, et al., "Fatigue Response of As-Built DMLS Maraging Steel and Effects of Aging, Machining, and Peening Treatments," *Metals (Basel).* 8 (2018): 8.

29. D. Croccolo, S. Ćirić-Kostić, M. De Agostinis, et al., "Effect of the Position in the Build Chamber on the Fatigue Strength of Additively Manufactured Maraging Steel MS1," *Machines.* 11 (2023): 1–17.

30. EOS, "Maraging Steel Datasheet," accessed March 15, 2024. https://www.eos.info/05-datasheet-images/Assets_MDS_Metal/EOS_MaragingSteel_MS1/Material_DataSheet_EOS_MaragingSteel_MS1_EOSM290_EOSM290400W_EOSM300-4_EOSM400_EOSM400-4_en.pdf.

31. ISO, "ISO 1143 : 2010 BSI Standards Publication Metallic Materials — Rotating bar Bending Fatigue Testing," (2010).

32. ASTM, "E18-22 Standard Test Methods for Rockwell Hardness of Metallic Materials 1, 2," 2022, 1–38.

33. "ISO 12107. INTERNATIONAL STANDARD Statistical Planning and Analysis of Data. ISO Stand," (2012).

34. F. G. Pascual and W. Q. Meeker, "Estimating Fatigue Curves With the Random Fatigue-Limit Model," *Technometrics* 41 (1999): 277–289.

35. R. D. Pollak and A. N. Palazotto, "A Comparison of Maximum Likelihood Models for Fatigue Strength Characterization in Materials Exhibiting a Fatigue Limit," *Probabilistic Engineering Mechanics* 24 (2009): 236–241.

36. P. Strzelecki, T. Tomaszewski, and J. Sempruch, "A Method for Determining a Complete S-N Curve Using Maximum International Conference Engineering Mechanics 2016 Maximum Likelihood Abstract : Keywords : Fatigue, Steel, High-cycles, S-N curve, Accelerated methods," (2016).

37. S. Lorén and M. Lundström, "Modelling Curved S-N Curves," *Fatigue and Fracture of Engineering Materials and Structures* 28 (2005): 437–443.

38. G. Olmi, M. Comandini, and A. Freddi, "Fatigue on Shot-Peened Gears: Experimentation, Simulation and Sensitivity Analyses," *Strain* 46 (2010): 382–395.

39. B. Van Hooreweder, D. Moens, R. Boonen, and P. Sas, "The Critical Distance Theory for Fatigue Analysis of Notched Aluminium Specimens Subjected to Repeated Bending," *Fatigue and Fracture of Engineering Materials and Structures* 35 (2012): 878–884.

40. D. Croccolo, M. De Agostinis, S. Fini, G. Olmi, N. Bogojevic, and S. Ciric-Kostic, "Effects of Build Orientation and Thickness of Allowance on the Fatigue Behaviour of 15–5 PH Stainless Steel Manufactured by DMLS," *Fatigue and Fracture of Engineering Materials and Structures* 41 (2018): 900–916.

41. B. Epstein, "Introduction to Statistical Analysis (WJ Dixon and FJ Massey, Jr.)," *SIAM Review* 1 (1959): 75–77.

42. G. Olmi and A. Freddi, "A new Method for Modelling the Support Effect Under Rotating Bending Fatigue: Application to Ti-6Al-4V Alloy, With and Without Shot Peening," *Fatigue and Fracture of Engineering Materials and Structures* 36 (2013): 981–993.

43. I. H. ZainElabdeen, L. Ismail, O. F. Mohamed, K. A. Khan, and A. Schiffer, "Recent Advancements in Hybrid Additive Manufacturing of Similar and Dissimilar Metals via Laser Powder bed Fusion," *Materials Science and Engineering: A* 909 (2024): 146833.

44. Z. Pan, V. K. Nadimpalli, C. V. Funch, et al., "Microstructural Evolution of Multilayered AISI 316L-440C Steel Composites Manufactured by Laser Powder bed Fusion," *Materials Characterization* 211 (2024): 113907.

45. C. J. Bettencourt and N. Kouraytem, "Microstructural Characterization of the Transition in SS316L and IN625 Bimetallic Fabricated Using Hybrid Additive Manufacturing," *Journal of Metals* 75 (2023): 5079–5087.

46. Z. Wu, A. E. Wilson-Heid, R. J. Griffiths, and E. S. Elton, "A Review on Experimentally Observed Mechanical and Microstructural Characteristics of Interfaces in Multi-Material Laser Powder Bed Fusion," *Frontiers of Mechanical Engineering* 9 (2023): 1–20.